Heliyon 9 (2023) e23109

Contents lists available at ScienceDirect

Heliyon

journal homepage: www.cell.com/heliyon

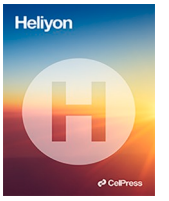

SERS and machine learning based effective feature extraction for detection and identification of amphetamine analogs

Jing Cai [a], Yulun Wu [a], Haohao Bai [a], Yingsheng He [b,**], Yazhou Qin [a,*]

[a] Key Laboratory of Drug Prevention and Control Technology of Zhejiang Province, Zhejiang Police College, 555 Binwen Road, Binjiang District, Hangzhou, 310053, Zhejiang Province, PR China
[b] Key Laboratory of Drug Control and Monitoring, National Anti-Drug Laboratory Zhejiang Regional Center, 555 Binwen Road, Binjiang District, Hangzhou, 310053, Zhejiang Province, PR China

ARTICLE INFO

Keywords:
Methamphetamines
Raman
SERS
DFT
Machine learning

ABSTRACT

Surface-enhanced Raman spectroscopy (SERS) is extensively researched in diverse disciplines due to its sensitivity and non-destructive nature. It is particularly considered a potential and promising technology for rapid on-site screening in drug detection. In this investigation, a technique was developed for fabricating nanocrystals of Ag@Au SNCs. Ag@Au SNCs, as the basic material of SERS, can detect amphetamine at concentrations as low as 1 μg/mL. The Ag@Au SNCs exhibits a strong surface plasmon resonance effect, which amplifies molecular signals. The SERS spectra of ten substances, including amphetamine and its analogs, showed a strong peak signal. To establish a qualitative distinction, we examined the Raman spectra and conducted density functional theory (DFT) calculations on the ten aforementioned species. The DFT calculation enabled us to determine the vibrational frequency and assign normal modes, thereby facilitating the qualitative differentiation of amphetamines and its analogs. Furthermore, the SERS spectrum of the ten mentioned substances was analysed using the support vector machine learning algorithm, which yielded a discrimination accuracy of 98.0 %.

1. Introduction

From the 2022 World Anti-Drug Report, seizures of amphetamine-type stimulants increased 15 % year-on-year in 2020, continuing the upward trend seen between 2010 and 2020. During this 10-year period, methamphetamine (METH) seizures increased fivefold, amphetamine seizures nearly quadrupled, and "ecstasy" seizures more than tripled, METH still dominates [1]. Amphetamine-type stimulants belong to a class of drugs that stimulate the central nervous system and have become the second most consumed illicit drug worldwide [2]. The abuse of even small amounts of amphetamine-type stimulants poses a serious threat to both physical and mental health, potentially leading to fatal outcomes.

Traditional detection methods for amphetamine-type stimulants primarily include gas chromatography-mass spectrometry [3–5], ion mobility spectrometry [6], high performance liquid chromatography-mass spectrometry [7–10], and enzyme-linked immunosorbent assay [11]. While these techniques demonstrate excellent sensitivity and precision, they typically necessitate intricate preprocessing procedures and costly instruments. Moreover, they often require significant detection time and the expertise of trained

* Corresponding author.
** Corresponding author.
E-mail addresses: 21537047@zju.edu.cn (Y. He), yazhouqin@zju.edu.cn (Y. Qin).

https://doi.org/10.1016/j.heliyon.2023.e23109
Received 13 November 2023; Received in revised form 25 November 2023; Accepted 27 November 2023
Available online 30 November 2023

personnel for data analysis. Consequently, a practical, fast, and highly sensitive detection technology is urgently needed.

In the past few years, SERS has garnered significant attention across multiple domains, encompassing food safety [12–15], biomedicine [16–20], environmental surveillance [21–23], and public security [24–27]. This technique offers several advantages such as no sample pre-treatment, fast detection speed, low cost, environmental friendliness, and the ability to provide rich information. It is particularly useful for on-site detection. The enhancement of SERS signals is predominantly accomplished via the distinct local characteristics of surface plasmon resonance exhibited by the nanostructure of the substrate materials. When exposed to the optical field, the plasmon resonance on the nanomaterial surface significantly enhances the electromagnetic field, thereby increasing the Raman signal intensity of the molecule being tested within a 5 nm range from the nanoparticle surface [28–30]. In recent decades, extensive research has focused on the synthesis of nanomaterials for substrate preparation, aiming to achieve remarkable enhancement effects. An ideal substrate material for SERS should exhibit strong localized surface plasmon resonance, dense SERS active sites or 'hot spots,' and good stability. Studies have consistently demonstrated that noble metal nanomaterials, such as Au (Au) and silver (Ag), generally exhibit superior localized surface plasmon resonance effects. Specifically, Ag nanocrystals have been found to provide approximately 100 times greater SERS enhancement compared to Au spheres of the same size, while Au nanocrystals exhibit better biocompatibility and stability than Ag nanocrystals [31]. Furthermore, the morphology of nanocrystals significantly influences the SERS enhancement. Various morphologies, including polyhedrons, spheres, rods, sea urchins, and nuclear satellites, have been successfully synthesized and investigated. Among them, the spiked structure contains more tip structures to form 3D SERS hot spots, which can further enhance the molecular signal to be detected [32,33]. For instance, Yan conducted a study using multi-branched Au NCs that had the ability to be tuned for localized surface plasmon resonance properties and embedded them in polydimethylsiloxane as a SERS substrate material for quantitative analysis of heme in red blood cells. They achieved a detection concentration as low as 0.03 nM without the need for hemoglobin separation [34]. Similarly, Fang et al. employed electrochemical deposition to prepare Au nano substrates with layered spikes for SERS detection of crystal violet and rhodamine 6G. The lowest detection concentrations achieved were 10^{-10} M and 10^{-11} M, respectively [35].

Several studies have reported the use of SERS for detecting illicit drugs, specifically amphetamine-type drugs. For instance, He et al. employed electrostatically assisted self-assembly of Au nanorods and silicon spheres to manipulate the photo plasmon resonance of hybrid materials. By adjusting the aspect ratio of Au nanorods, they optimized the local plasmon-photon according to the incident wavelength, resulting in enhanced electric field and the detection limit of methamphetamine (METH) is 5 nM [36]. The detection limit for methamphetamine in wastewater was achieved to be 0.01 ppb by Li and co-workers by implementing core-shell Au@Ag NCs on a substrate made of glass nanofiber paper, serving as a SERS substrate. This enabled wastewater-based epidemiological toxicity monitoring [37]. Additionally, Shen et al. employed SERS for on-site rapid and highly sensitive detection of METH in human blood and urine [38]. However, it is worth noting that most of the current research focuses on SERS detection of METH, with limited studies on detecting other amphetamine-type substances.

In this work, we first performed conventional Raman detection on 10 different types of amphetamine analogs to obtain their Raman spectra. Subsequently, we developed Ag@Au spik nanocrystals (Ag@Au SNCs) using the seed mediate synthesis method. These Ag@Au SNCs effectively capitalizes on the advantages of both Au and Ag nanocrystals, as well as the 3D hotspot distribution of the spiked structure, making them exceptional SERS substrate materials. We utilized the Ag@Au SNCs as a SERS substrate material for detecting 10 different types of amphetamine analogs, including Admphetamine hydrochloride (AMP), methamphetamine hydrochloride (METH), Ephedrine hydrochloride (EPH), 4-Propylthio-2,5- dimethoxyphenethylamine hydrochloride (2C-T-7), 4-Chloro-2,5-dimethoxyphenethylamine hydrochloride (2C–C), 4-Ethyl-2,5-dimethoxyphenethylamine hydrochloride (2C-E), N-Methyl-1-(4-methoxyphenyl)propan-2-amine hydrochloride (PMMA), N-Methyl-1-(4-fluorophenyl)propan-2-amine hydrochloride (4-FMA), N-Methyl-1-(benzofuran-5-yl)propan-2-amine hydrochloride (5-MAPB), Methylenedioxypyrovalerone hydrochloride (MDPV). We successfully achieved trace detection of these substances. To further analyze the Raman spectra, we employed density functional theory (DFT) to calculate the vibration peaks and assigned them accordingly, enabling qualitative distinction. Furthermore, we realized the rapid identification of SERS spectra of 10 substances by principal component analysis and machine learning algorithm, with 98.0 % accurate.

2. Materials and methods

2.1. Materials

Chemicals used in this study included hexadecyltrimethylammonium bromide (AR, 99 %), glutathione (Mw = 307.32, ≥98 %), hydrochloroauric acid trihydrate ($HAuCl_4{\cdot}3H_2O$, 99.9 %). Silver nanocube (80 nm, >99 %, 0.1 mg/mL) were purchased from NANO Lab. Amphetamine hydrochloride (AMP), methamphetamine hydrochloride (METH), Ephedrine hydrochloride (EPH), 4-Propylthio-2,5- dimethoxyphenethylamine hydrochloride (2C-T-7), 4-Chloro-2,5-dimethoxyphenethylamine hydrochloride (2C–C), 4-Ethyl-2,5-dimethoxyphenethylamine hydrochloride (2C-E), N-Methyl-1-(4-methoxyphenyl)propan-2-amine hydrochloride (PMMA), N-Methyl-1-(4-fluorophenyl)propan-2-amine hydrochloride (4-FMA), N-Methyl-1-(benzofuran-5-yl)propan-2-amine hydrochloride (5-MAPB), Methylenedioxypyrovalerone hydrochloride (MDPV) standards were all purchased from the Shanghai Institute of Criminal Science and Technology (Shanghai, China). The solutions were prepared from pure water (18 MΩ cm) purified through a Milli-Q Lab system (Nihon Millipore Ltd.). The glass instruments used in the experiment were all cleaned with newly configured aqua regia for 30 min, then washed twice with ultrapure water and ethanol respectively, and then dried in an oven for use.

2.2. Synthesis of Ag@Au SNCs

Ag@Au SNCs was synthesized using a slightly modified version of our previously reported method [27]. Firstly, add 0.07 g CTAB to the glass bottle along with 20 mL of water, and the solution was stirred magnetically at 500 rpm for 10 min. Next, 0.2 mL of 10 mM $HAuCl_4 \blacksquare 3H_2O$ was added to the CTAB solution and stirred magnetically for 10 min. Next, the solution was supplemented with 475 μL of a reducing agent, consisting of 100 mM ascorbic acid. Subsequently, 0.4 mL of 80 nm Ag seed and 0.1 mL of 1 mM glutathione solution were introduced into the system, followed by stirring the mixture for a duration of 2 h, resulting in the formation of Ag@Au SNCs. The resulting Ag@Au SNCs was centrifuged at 8000 rpm to remove the supernatant, washed three times with ethanol and water, respectively, and stored in ultrapure water for future use. To prepare Ag@Au nanocrystals with varying morphologies, we kept all other reaction conditions constant and only adjusted the amount of glutathione to 20 μL, 100 μL, and 200 μL.

2.3. Raman and SERS characterization

In this experiment, the standard powders of 10 analytes were picked up using a capillary. The capillary was then fixed on a glass slide using double-sided tape. The diagonal powder samples were tested under a confocal microscope. For SERS testing, a 1 mg/mL standard solution was prepared. To prepare the solution, 10 μL of the standard solution of amphetamine analogs and 10 μL of Ag@Au SNCs were mixed and shaken well for 5 min. Following that, the glass slide was subjected to dropwise addition of 5 μL of the nanoparticle solution. Subsequently, the solution was allowed to dry at room temperature before conducting the SERS test. The Raman test employed a 633 nm laser with a power of 6.0 mW, an exposure time of 10 s, and a magnification of 50 times using the objective lens (OLYMPUS 50× 0.75 BD). The results of the SERS test align with those obtained from the Raman analysis.

2.4. Instrumentation and characterization

Ag@Au SNCs was characterized using the Hitachi HT7700 transmission electron microscopy at 100 kV. The Raman and SERS characterization was performed using the Thermo Fisher DXR2xi confocal Raman spectrometer. To obtain the standard powder for Raman testing, a capillary stick was utilized. For the Raman test, a laser with a wavelength of 633 nm, emitting a power of 6.0 mW, while being exposed for 10 s, and viewed through an objective lens with a magnification of 50 times, was utilized. The SERS test exhibited similar findings to the Raman test. To prepare the experimental equipment, all glassware underwent a 30-min cleaning process using aqua regia, followed by thorough rinsing with water and ethanol, and eventual drying for future utilization.

2.5. Computational methods

Amphetamine-like substances were calculated using Gaussian 09 software. The B3LYP/6–311++G(d,p) method was employed for

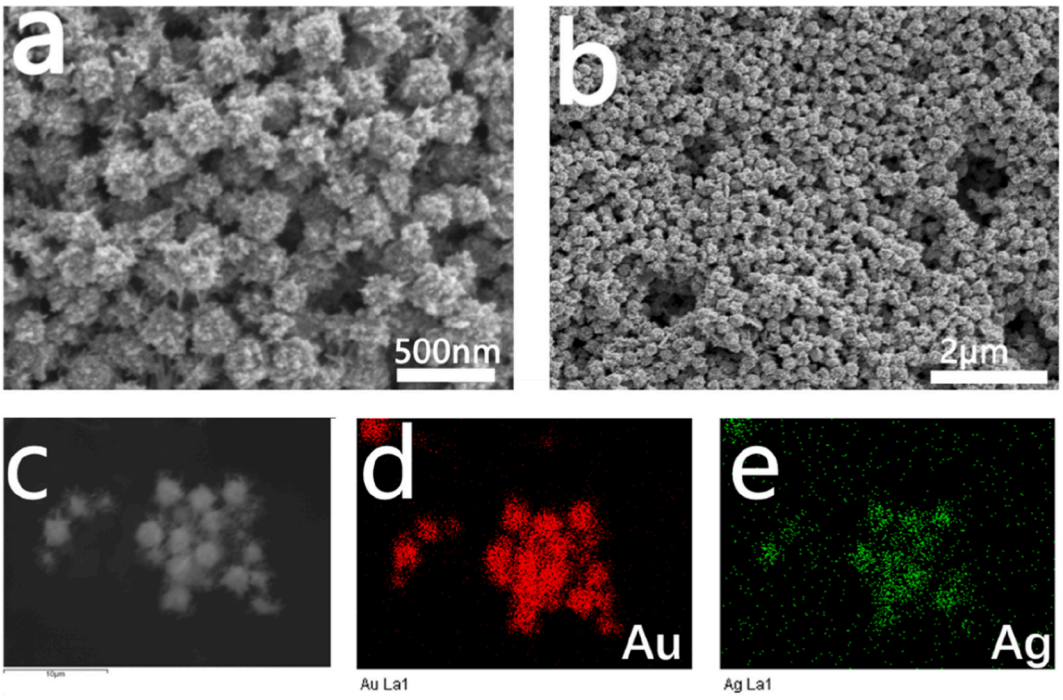

Fig. 1. (a–b) SEM images of Ag@Au SNCs. (c–e) Are the corresponding EDS images of Au and Ag.

the calculation, and the structure was optimized prior to the calculation. The harmonic approximation of the theoretical model introduces errors that can be corrected using scale factors.

2.6. Data analysis

We collected a total of 500 spectral data points by utilizing a 633 nm laser, which operated at a power of 6.0 mW for an exposure duration of 10 s. Each group comprises 50 individual data points. To eliminate any interference caused by noise, we subjected the data to pre-processing. The Raman device, OMNIC for Dispersive Raman, provided the necessary software for this task. Using MATLAB software from Mathworks in the USA, we further normalized the spectrum after removing the baseline. Additionally, we applied a dimension reduction technique called PCA to reduce the data's dimensionality.

We utilized support vector machine (SVM) to showcase the classification outcomes. The classifiers were trained on a dataset consisting of 25 samples and subsequently tested on another dataset containing 25 samples. Pytorch 1.1.0 was employed as the backend for implementing the classification models. During the training phase, we set the values of C = 10, kernel = 'Linear', gamma = 'scale', and random state = 42. Furthermore, we incorporated PCA with 9 components as the configuration for the SVM model. After the training process was finished, we documented the outcomes of the confusion matrix executed by the classifier on the test set for comparative analysis. In order to further optimize the classification accuracy of support vector machine, we use the method of grid search for optimal parameters to adjust and optimize the penalty factor C and degree parameters under poly kernel function.

3. Results and discussion

3.1. Characterization of the prepared Ag@Au SNCs

The Ag seeds were first characterized, as shown in Fig. S1, which is a transmission electron micrograph revealing their cubic structure with regular edge lengths of 80 nm. Subsequently, the as-prepared Ag@Au nanocrystals were characterized using scanning electron microscopy, as depicted in Fig. 1. Fig. 1a and b presents high and low magnification SEM images of the as-prepared Ag@Au nanoparticles, respectively. As we can see that the as-prepared nanocrystals exhibit a spike morphology, with a central core size of approximately 150 nm and numerous dense spiked structures on the outer shell. The element distribution energy spectra (Fig. 1c, d and e) confirm that the Ag@Au nanoparticles are composed of Au and silver. The spiked structure of the Ag@Au nanocrystals facilitates the growth of Au on the outer surface of the Ag spheres. Compared to solid nanocrystals, the spiked structure exhibits a significant enhancement of the electromagnetic field at the tip of the branch and the nanogap between the branches. For instance, Ha et al. conducted finite-difference time-domain (FDTD) simulations and observed a strong electric field distribution at the tip of a nanoparticle [39]. Additionally, Wang et al. demonstrated that increasing the density of the branches and shortening the distance of the nanogap can greatly enhance the electromagnetic field intensity within the nanogap [40]. The Ag@Au spiked structure not only utilizes the localized surface plasmon resonance properties of Ag nanoparticles but also benefits from the external Au, which enhances the stability of the prepared Ag@Au spiked structure. Moreover, in the case of Ag@Au SNCs with spiked structure, both the inner Ag seed and the outer Au dense spiked structure contribute to the SERS enhancement effect, while the gap between them forms an overlapping area of electric field enhancement, resulting in a 3D hot spot with higher SERS.

The effect of the ligand glutathione on the prepared nanocrystals was investigated. Fig. 2 shows the nanocrystals prepared with different morphologies by varying the amount of glutathione to 20 μL, 100 μL, and 200 μL, while the other conditions remain

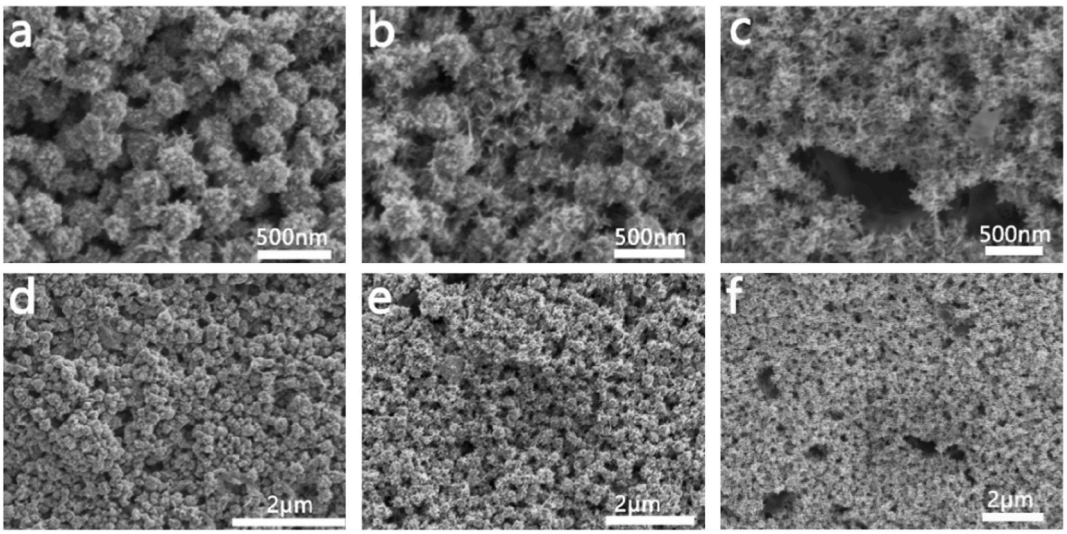

Fig. 2. SEM images of Ag@Au SNCs prepared with different GSH. (a, d) 20 μL, (b, e) 100 μL (c, f) 200 μL.

unchanged. In Fig. 2a and d, the SEM image of the nanocrystals prepared with 20 μL of GSH reveals the presence of numerous small particles growing on the surface of the Ag cube, with only a few shorter spikes formed. By increasing the amount of GSH to 100 μL, Ag@Au nanocrystals with spiked structures on the surface can be obtained (Fig. 2b and e). It is evident that a significant number of spiky structures grow on the surface of the seeds. Further increasing the GSH to 200 μL leads to denser spiked structures on the surface of Ag cubes (Fig. 2c and f), completely covering the surface of the seeds with spikes. Based on these experimental observations, it can be inferred that glutathione initially binds to the seed and adsorbs onto the surface of the silver cube seed. Subsequently, upon adding the Au precursor solution, Au^{+} combines with glutathione through an Au–S bond [24], resulting in Au growth along the molecular direction of glutathione. When a smaller amount of glutathione is added, only a few Au thorn structures are formed, whereas adding more glutathione leads to the formation of a greater number of Au thorn structures.

3.2. Raman and SERS characterization

We utilized Ag@Au NCs with densely spiked structures on the surface as the substrate material for SERS testing. To eliminate any potential interference from ligands on the surface of Ag@Au NCs, we performed SERS characterization. Fig. S2 demonstrates that Ag@Au NCs did not exhibit any significant SERS characteristic peak, suggesting that there would be no interference in the test. We first evaluated the detection performance of the SERS substrate using rhodamine 6G (R6G) molecules with a large cross-sectional area as the analyte, as shown in Fig. S3. The minimum detectable concentration of R6G was 10^{-9} M. Furthermore, the uniformity of the detection substrate was characterized by randomly selecting 10 sites. The relative standard deviations of the peaks at 613 cm^{-1} and 1362 cm^{-1} were 7.3 % and 11.2 %, respectively, indicating that the SERS detection method has good uniformity. And the methamphetamine and their analogs used in this research including Amphetamine hydrochloride (AMP), Methylamphetamine hydrochloride (METH), Ephedrine hydrochloride (EPH), 4-Propylthio-2,5-dimethox-phenethylamine hydrochloride (2C-T-7), 4-Chloro-2,5-dimethoxyphenethylamine hydrochloride (2C–C), 4-Ethyl-2,5-dimethoxyphenethylamine hydrochloride (2C-E), N-Methyl-1-(4-methoxyphenyl) propan-2-amine hydrochloride, (PMMA) N-Methyl-1-(4-fluorophenyl) propan-2-amine hydrochloride (4-FMA), N-Methyl-1-(benzofuran-5-yl) propan-2-amine hydrochloride (5-MAPB), Methylenedioxypyrovalerone hydrochloride (MDPV), and the chemical structures are shown in Fig. 3. We can see that these molecules have a similar backbone structure to amphetamines. Initially, we conducted Raman, SERS, and DFT theoretical spectral calculations for the aforementioned substances. Fig. 4A illustrates the Raman, SERS, and DFT of amphetamine, demonstrating a good agreement between the characteristic peaks observed in the obtained results. Table S1 presents the main characteristic peaks observed in the SERS spectrum of amphetamine, along with the corresponding peaks calculated using Raman and DFT. The correction factor for the DFT calculated spectra is determined to be 0.9843. The vibrational peak at 622 cm^{-1} is contributed by the in-plane bending vibration of the benzene ring and the bending vibration of the C–C bond in the amphetamine molecule. The characteristic peak at 1003 cm^{-1} is the breathing vibration of the benzene ring. And the characteristic peaks at 1032 cm^{-1} are the stretching vibration of C–C and C–N and the rocking vibration of N–H. 1208 cm^{-1} and 1602 cm^{-1} are the characteristic peaks of rocking vibration of N–H, C–H, and the characteristic peak of the stretching vibration of C═C, rocking vibration of C–H on the benzene ring, respectively. Additionally, we utilized Ag@Au NCs with a dense spiked structure on the surface as the substrate material for conducting SERS testing on amphetamines with various concentrations. Fig. 4b presents the SERS spectra of

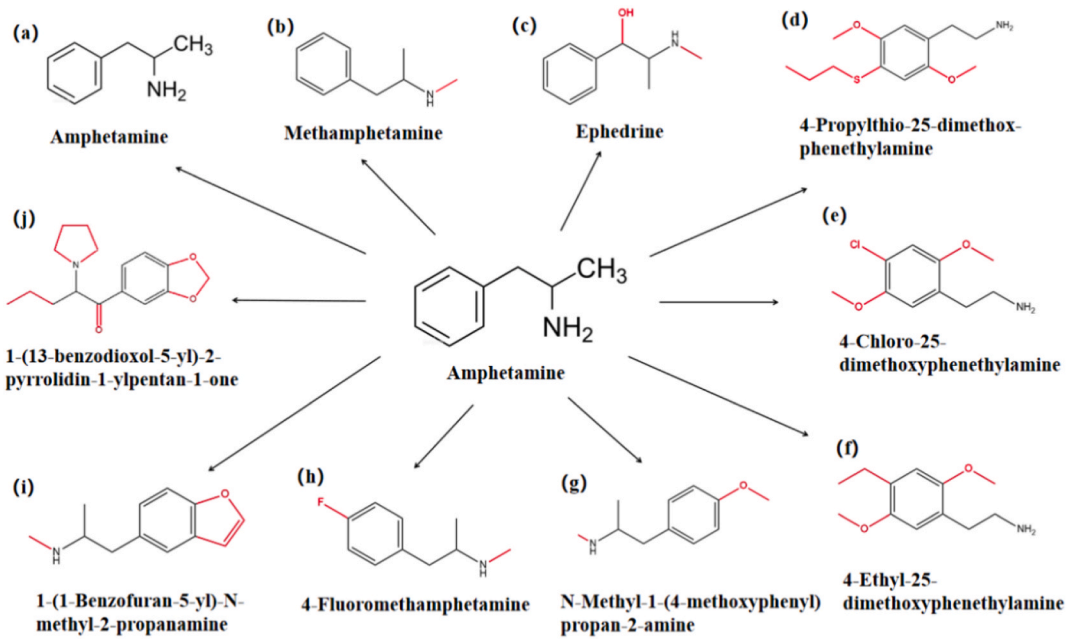

Fig. 3. Chemical structures of amphetamine and its analogs.

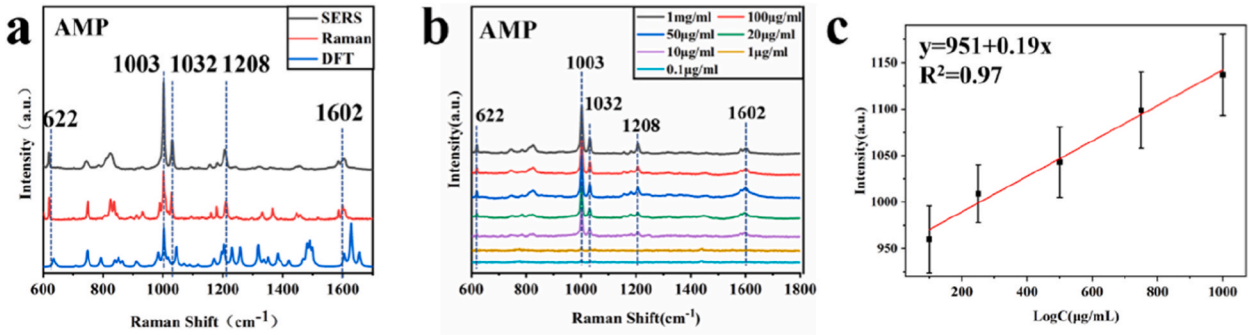

Fig. 4. (a) Raman, SERS and DFT of amphetamine. (b) SERS spectra of amphetamines at different concentrations. (c) Scatter plots and linear fitting.

amphetamines ranging from 1 mg/mL to 0.1 μg/mL. The trace detection of amphetamine is achieved with a lowest detectable concentration of 1 μg/mL, which is close to the detection level reported in existing literature. Moreover, we used the peak intensity at 1083 cm^{-1} as a function of the AMP concentration to plot the linear fit, and the results are shown in Fig. 4c. We see a linear correlation between peak intensity and concentration in the range of 100–1000 μg/mL, and the correlation coefficient R^2 is 0.97.

Fig. 5 displays the Raman, SERS, and DFT calculated spectra of nine amphetamine analogs. Tables S2–S10 provides the corresponding Raman, SERS, and DFT calculation spectrum peak assignments for the 9 amphetamine analogs. The Raman and SERS peak

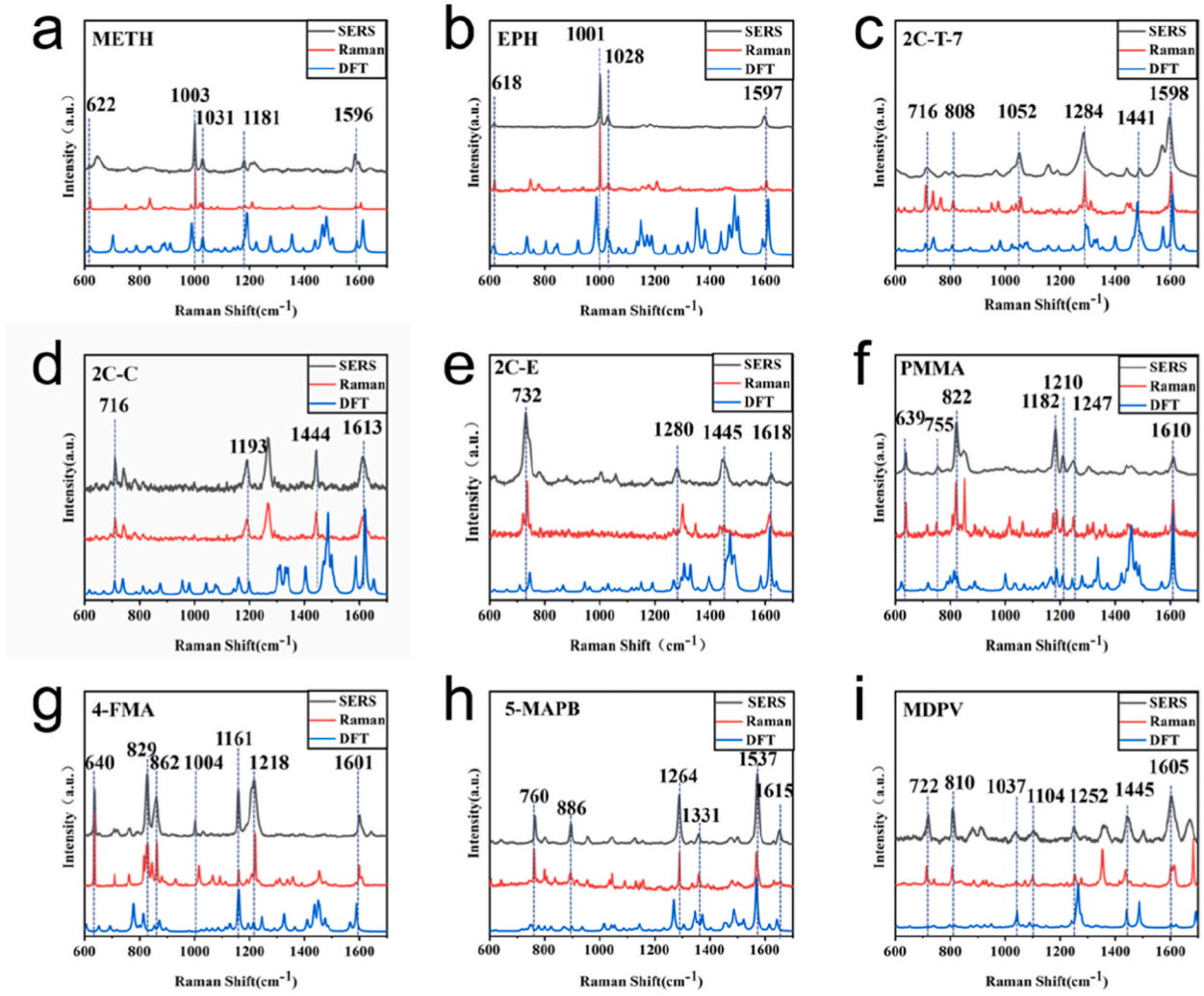

Fig. 5. Raman, SERS and DFT of amphetamine analogs.

positions of the aforementioned 10 substances are largely identical. The SERS characteristic peaks of METH (Fig. 5a) are located at 622 cm^{-1}, 1003 cm^{-1}, 1031 cm^{-1}, 1181 cm^{-1} and 1596 cm^{-1}, which correspond to the in-plane bending, ring breathing, stretching vibration of C═C bond, the rocking vibration of the C–H bond of the methyl group and the rocking vibration of the C–H bond of the benzene ring. The SERS characteristic peaks of EPH (Fig. 5b) are located at 618 cm^{-1}, 1001 cm^{-1}, 1028 cm^{-1} and 1597 cm^{-1}, which correspond to the in-plane bending, ring breathing, stretching vibration of the C═C bond and the rocking vibration of the C–H bond of the benzene ring, respectively. The SERS characteristic peaks of 2C-T-7 (Fig. 5c) are located at 716 cm^{-1}, 808 cm^{-1}, 1052 cm^{-1}, 1284 cm^{-1}, 1441 cm^{-1} and 1598 cm^{-1}, corresponding to the out-of-plane bending of the benzene ring, rocking vibration of the C–H bond in CH_2, stretching vibration of C–O bond, stretching vibration of C–*O*–C bond, wagging vibration of C–H bond in CH_2 and rocking vibration of C–H bond in benzene ring, respectively. The SERS characteristic peaks of 2C–C (Fig. 5d) are located at 716 cm^{-1}, 1193 cm^{-1}, 1444 cm^{-1} and 1613 cm^{-1}, corresponding to the out of plane bending of the benzene ring, the rocking vibration of the C–H bond in CH_3, the rocking vibration of the C–H bond in CH_2 and the rocking vibration of the C–H bond in the benzene ring, respectively. The SERS characteristic peaks of 2C-E (Fig. 5e) are located at 732 cm^{-1}, 1280 cm^{-1}, 1445 cm^{-1} and 1618 cm^{-1}, corresponding to the in-plane bending of the benzene ring, the rocking vibration of the C–H bond in the benzene ring, the rocking vibration of the C–H bond in CH_2 and the stretching vibration of the C═C bond in the benzene ring, respectively. The SERS characteristic peaks of PMMA (Fig. 5f) are located at 639 cm^{-1}, 822 cm^{-1}, 1182 cm^{-1}, 1210 cm^{-1}, 1247 cm^{-1} and 1610 cm^{-1}, corresponding to the in-plane bending of the benzene ring, the out-of-plane of the benzene ring, the rocking vibration of the C–H bond in the benzene ring, the ring breathing of the benzene ring, the stretching vibration of the C–*O*–C and the stretching vibration of the C═C bond in the benzene ring respectively. The SERS characteristic peaks of 4-FMA (Fig. 5g) are located at 640 cm^{-1}, 829 cm^{-1}, 862 cm^{-1}, 1004 cm^{-1}, 1161 cm^{-1}, 1218 cm^{-1} and 1601 cm^{-1}, which correspond to the in-plane bending of the benzene ring, the wagging vibration of the benzene ring, rocking vibration of C–C bond, stretching vibration of C–C bond, rocking vibration of C–H bond in benzene ring, ring breathing vibration of benzene ring and stretching vibration of C═C bond in benzene ring, respectively. The SERS characteristic peaks of 5-MAPB (Fig. 5h) are located at 760 cm^{-1}, 886 cm^{-1}, 1264 cm^{-1}, 1331 cm^{-1}, 1537 cm^{-1} and 1615 cm^{-1}, corresponding to the out-of-plane bending of the benzene ring, the rocking vibration of the C–H bond in CH_2, the ring breathing vibration of the benzene ring, the rocking vibration of the C–H bond in the furan ring, the stretching vibration of the C═C bond in the furan ring and the stretching vibration of the C═C bond in the benzene ring, respectively. The SERS characteristic peaks of MDPV (Fig. 5i) are located at 722 cm^{-1}, 810 cm^{-1}, 1037 cm^{-1}, 1104 cm^{-1}, 1252 cm^{-1}, 1445 cm^{-1} and 1605 cm^{-1}, which correspond to the rocking vibration of the C–H bond in CH_2, the wagging vibration of the C–H bond, The stretching vibration of the C═C bond in the benzene ring, the rocking vibration of the C–H bond of the benzene ring, the stretching vibration of the C═C bond in the benzene ring and the stretching vibration of the C═O bond, respectively.

In Fig. 6a, it is evident that among the 10 species mentioned, the dominant peaks with the highest intensity are observed at 1002 cm^{-1} for AMP, METH, and EPH. AMP stands out with distinct characteristic peaks at 827 cm^{-1} and 1332 cm^{-1}, which differentiate it from METH and EPH. Additionally, METH can be distinguished from EPH by its unique characteristic peak at 840 cm^{-1}. The characteristic peaks of 2C-T-7, 2C–C, and 2C-E, which are distinct from other substances, appear at 1289 cm^{-1}, 1295 cm^{-1}, and 1303 cm^{-1}, respectively, showcasing noticeable C–*O*–C in-plane bending vibration characteristics. PMMA and 4-FMA differ in terms of their characteristic peaks. The stretching vibration of the C–*O*–C bond in PMMA occurs at 1247 cm^{-1}, while the stretching vibration of the C–F bond in 4-FMA occurs at 1163 cm^{-1}. 5-MAPB exhibits a characteristic peak at 1538 cm^{-1} due to the presence of a furan ring. Notably, MDPV stands apart from other substances with its distinct and prominent characteristic peak at 1684 cm^{-1}, which corresponds to the C═O stretching vibration.

For the SERS data of the 10 substances mentioned above (Fig. 6b), we utilized machine learning algorithms for classification and identification. In the field of machine learning, the assessment metrics can vary in terms of dimensions and units, potentially impacting the outcomes of data analysis. To address this issue, data standardization is necessary to ensure comparability among the indicators. By standardizing the original data, all indicators are adjusted to the same order of magnitude, enabling comprehensive comparative

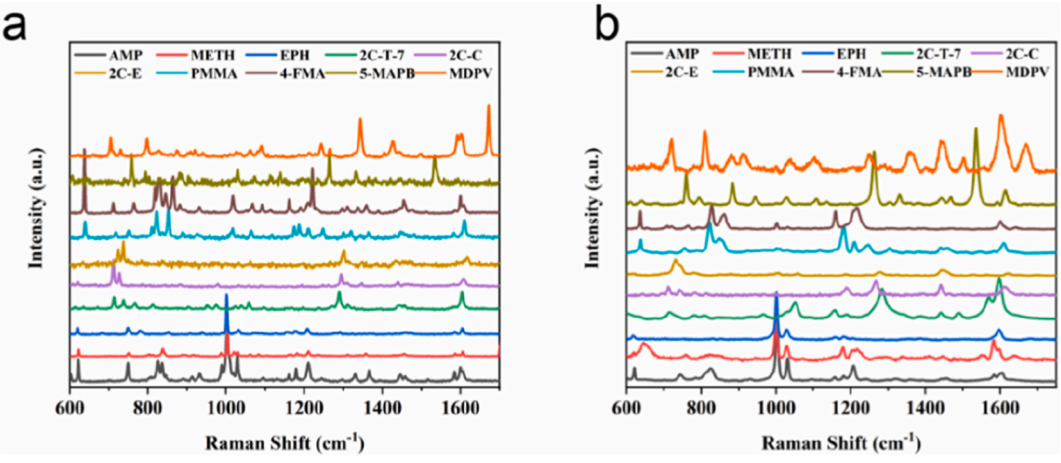

Fig. 6. Raman (a) and SERS spectra (b) of amphetamine analogs.

evaluation. To ensure consistent peak levels and eliminate noise interference, we initially corrected the baseline of the measured data. The data was then grouped under different measurement conditions for each substance, using the same numbering as shown in Fig. 3 (encoded as a, b, c, d, e, f, g, h, i, j). In order to create a training and test set, we randomly divided 500 SERS spectral data into two equal parts. The first half was used as the training set, while the remaining half formed the test set. Additionally, we normalized the data to mitigate the adverse effects caused by sample differences. According to the results shown in Fig. 7, the cumulative variance contribution rate indicates that when the dimensionality reduction dimension is 9, the variance contribution rate exceeds 95 %, reaching 97 %. Therefore, it is recommended to select the first 9 principal components in order to achieve better classification accuracy. Afterwards, the data is trained and the test set data is predicted using the SVM machine learning algorithm. The accuracy of the classification is evaluated using a confusion matrix, as shown in Fig. 8a–d. The classification accuracy for the Polynomial Kernel, Sigmoid Kernel, Gaussian kernel and Linear Kernel are 60.4 %, 84.8 %, 88.4 % and 92.4 %, respectively. Therefore, the linear kernel function is used for training modelling, and the penalty factor C in the linear kernel function is further adjusted and optimized by using the five-fold cross-validation method. Table S11 is the accuracy of five-fold cross validation. It can be seen from Fig. 9 that when C increases from 0.001 to 10, the accuracy of the five-fold cross-validation gradually increases, and reaches the highest when C is 10, and then the accuracy decreases as C continues to increase and tends to be stable (the average classification accuracy is randomly taken 20 times). Table S12 shows the accuracy of changing the penalty factor C under different kernel functions. We can see that when the linear kernel function is selected and the penalty factor is 10, the highest accuracy is 98.0 %.

4. Conclusions

To recapitulate, we effectively fabricated Ag@Au doped nanocrystals (SNCs) exhibiting a dense three-dimensional hot spot distribution by utilizing 80 nm Ag cubes as initial seeds alongside hexadecyltrimethylammonium bromide and glutathione as directing agents. The reducing agent employed was ascorbic acid. This synthetic approach allows for the integration of superior properties from both Au and silver nanocrystals into the resulting SNCs. Furthermore, Ag@Au SNCs was utilized as the underlying material for SERS. Our investigation successfully attained trace detection of amphetamine and conducted regular detection of amphetamine analogs through Raman and SERS techniques. Moreover, we carried out DFT calculations on the Raman spectra of the aforementioned compounds. By integrating the normal Raman spectra, SERS data and DFT spectra of the above 10 substances, the characteristic peaks were successfully identified and qualitative identification was achieved. In addition, we used support vector machines to classify the SERS spectra of the above 10 substances, resulting in an impressive identification accuracy of 98.0 %.

Data availability statement

Data will be made available on request.

CRediT authorship contribution statement

Jing Cai: Writing – original draft, Methodology, Investigation, Funding acquisition, Conceptualization. **Yulun Wu:** Writing – original draft, Investigation, Formal analysis, Data curation. **Haohao Bai:** Writing – original draft, Investigation, Formal analysis, Data curation. **Yingsheng He:** Writing – review & editing, Writing – original draft, Investigation, Data curation, Conceptualization. **Yazhou Qin:** Writing – review & editing, Writing – original draft, Methodology, Funding acquisition, Formal analysis, Data curation, Conceptualization.

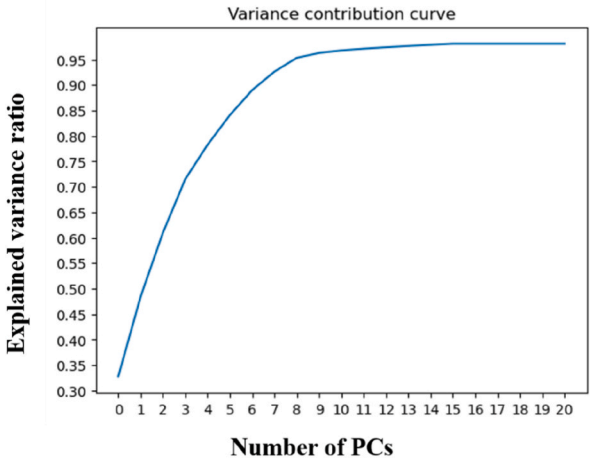

Fig. 7. The contribution rate of the principal component characteristic variance.

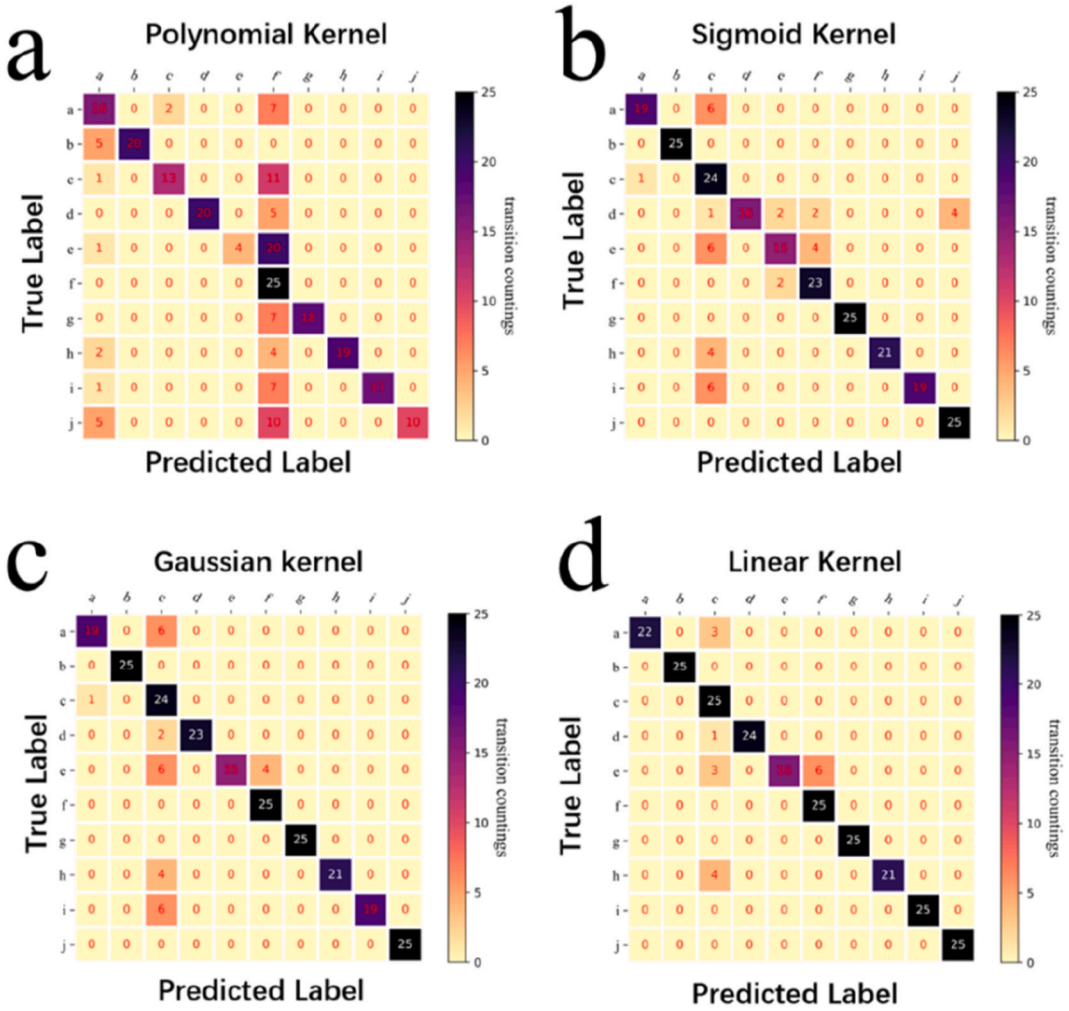

Fig. 8. Confusion matrix of SVM with different kernel. (a) Polynomial, (b) Sigmoid, (c) Gaussian and (d) Linear.

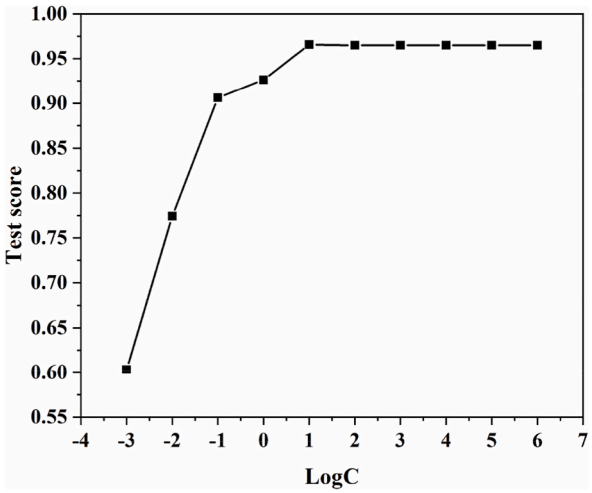

Fig. 9. The curve of the average accuracy of five-fold cross-validation with the penalty factor C.

Declaration of competing interest

The authors declare that they have no known competing financial interests or personal relationships that could have appeared to influence the work reported in this paper.

Acknowledgements

The support for this study was provided by the National Key R&D Program of China (2023YFC3303901) and the Key Research and Development Project of Zhejiang Province (2021C03135).

Appendix A. Supplementary data

Supplementary data to this article can be found online at https://doi.org/10.1016/j.heliyon.2023.e23109.

References

[1] World Drug Report, UNODC (United Nations Office on Drugs and Crime), 2022. Available at: https://www.unodc.org/res/wdr2022/MS/WDR22.
[2] Q. Shi, Y. Shi, Y. Pan, Z. Yue, H. Zhang, C. Yi, Colorimetric and bare eye determination of urinary methylamphetamine based on the use of aptamers and the salt-induced aggregation of unmodified Au nanocrystals, Microchim. Acta 182 (3) (2015) 505–511.
[3] K. Okajima, A. Namera, M. Yashiki, I. Tsukue, T. Kojima, Highly sensitive analysis of methamphetamine and amphetamine in human whole blood using headspace solid-phase microextraction and gas chromatography–mass spectrometry, Forensic Sci. Int. 116 (1) (2001) 15–22.
[4] J. Welter, M.R. Meyer, E.U. Wolf, 2-Methiopropamine, a thiophene analogue of methamphetamine: studies on its metabolism and detectability in the rat and human using GC-MS and LC-(HR)-MS techniques, Anal. Bioanal. Chem. 405 (10) (2013) 3125–3135.
[5] K. Zaitsu, M. Katagi, M. Tatsuno, Recently abused β-keto derivatives of 3, 4-methylenedioxyphenylalkylamines: a review of their metabolisms and toxicological analysis, Forensic Toxicol. 29 (2) (2011) 73–84.
[6] M.L. Ochoa, P.B. Harrington, A. Chem, Detection of methamphetamine in the presence of nicotine using in situ chemical derivatization and ion mobility spectrometry, Anal. Chem. 76 (4) (2004) 985–991.
[7] S.E. Toker, Detection of methamphetamine, methylenedioxy methamphetamine, and 3, 4-methylenedioxy-N-ethylamphetamine in spiked plasma by HPLC and TLC, J. AOAC Int. 93 (2) (2010) 556–561.
[8] D.K. Wissenbach, M.R. Meyer, D. Remane, Drugs of abuse screening in urine as part of a metabolite-based LC-MS screening concept, Anal. Bioanal. Chem. 400 (10) (2011) 3481–3489.
[9] B. Subedi, K. Kannan, Mass loading and removal of select illicit drugs in two wastewater treatment plants in New York State and estimation of illicit drug usage in communities through wastewater analysis, Environ. Sci. Technol. 48 (12) (2014) 6661–6670.
[10] P. Du, K. Li, J. Li, Z. Xu, et al., Methamphetamine and ketamine use in major Chinese cities, a nationwide reconnaissance through sewagebased epidemiology, Water Res. 84 (2015) 76–84.
[11] N.V. Guteneva, S.L. Znoyko, A.V. Orlov, M.P. Nikitin, P.I. Nikitin, Rapid lateral flow assays based on the quantification of magnetic nanoparticle labels for multiplexed immunodetection of small molecules: application to the determination of drugs of abuse, Microchim. Acta 186 (9) (2019) 621.
[12] P.Y. Ma, F.H. Liang, D. Wang, Q.Q. Yang, Y.Y. Ding, Y. Yu, D.J. Gao, D.Q. Song, X.H. Wang, Ultrasensitive determination of formaldehyde in environmental waters and food samples after derivatization and using silver nanoparticle assisted SERS, Microchim. Acta 182 (2015) 863–869.
[13] B. Bai, X. Mao, J. Wei, Selective anion-responsive organogel based on a gelator containing hydrazide and azobenzene units, Sensor. Actuator. B Chem. 211 (2015) 268–274.
[14] J.K. Yang, H. Kang, H. Lee, Single-step and rapid growth of silver nanoshells as SERS-active nanostructures for label-free detection of pesticides, ACS Appl. Mater. Interfaces 6 (2014) 12541–12549.
[15] Y.J. Oh, M. Kang, M. Park, K.H. Jeong, Engineering hot spots on plasmonic nanopillar arrays for sers: a review, BioChip J 10 (4) (2016) 297–309.
[16] K.K. Maiti, A. Samanta, M. Vendrell, K.S. Soh, M. Olivo, Y.T. Chang, Multiplex cancer cell detection by SERS nanotags with cyanine and triphenylmethane Raman reporters, Chem. Commun. 47 (12) (2011) 3514–3516.
[17] B. Yan, Y. Hong, T.B. Chen, M. Reinhard, Monitoring enzymatic degradation of pericellular matrices through SERS stamping, Nanoscale 4 (13) (2012) 3917–3925.
[18] M.D. Hodges, J.G. Kelly, A.J. Bentley, et al., Combining immunolabeling and surface enhanced Raman spectroscopy on cell membranes, ACS Nano 5 (12) (2011) 9535–9541.
[19] J.A. Huang, M.Z. Mousavi, G. Giovannini, Multiplex discrimination of single amino acid residues in polypeptides by single SERS hot spot, Angew. Chem. Int. Ed. 28 (28) (2020) 11423–11431.
[20] J.L. Campbell, E.D. SoRelle, O. Ilovich, O. Liba, et al., Multimodal assessment of SERS nanoparticle biodistribution post ingestion reveals new potential for clinical translation of Raman imaging, Biomaterials 135 (2017) 42–52.
[21] Y.Z. Qin, J.X. Qiu, N. Tang, Y.Z. Wu, W.X. Yao, He YS Controllable preparation of mesoporous spike Au nanocrystals for surface-enhanced Raman spectroscopy detection of micro/nanoplastics in water, Environ. Res. 228 (2023) 115926–115936.
[22] M. Jiang, Z. Qian, X. Zhou, et al., CTAB micelles assisted rGO–Ag NP hybrids for SERS detection of polycyclic aromatic hydrocarbons, Phys. Chem. Chem. Phys. 17 (2015) 21158–21163.
[23] X. Zhang, Z. Dai, S. Si, et al., Ultrasensitive SERS substrate integrated with uniform subnanometer scale "hot spots" created by a graphene spacer for the detection of mercury ions, Small 13 (9) (2017) 1603347–1603354.
[24] Y.Z. Qin, S.S. Yin, M.J. Chen, W.X. Yao, Y.S. He, Surface-enhanced Raman spectroscopy for detection of fentanyl and its analogs by using Ag-Au nanoparticles, Spectrochim. Acta Mol. Biomol. Spectrosc. 285 (2023) 121923–121931.
[25] M. Zhang, J. Pan, X. Xu, et al., Au-Trisoctahedra-Coated capillary-based SERS platform for microsampling and sensitive detection of trace fentanyl, Anal. Chem. 94 (11) (2022) 4850–4858.
[26] Y.Z. Qin, Y.Z. Wu, B.J. Wang, J.Y. Wang, X. Zong, W.X. Yao, Controllable preparation of sea urchin-like Au SNCs as a SERS substrate for highly sensitive detection of the toxic atropine, RSC Adv. 11 (32) (2021), 19813.
[27] Y.Z. Qin, F. Mo, S. Yao, Y.Z. Wu, Y.S. He, W.X. Yao, Facile synthesis of porous Ag crystals as SERS sensor for detection of five methamphetamine analogs, Molecules 27 (2022) 3939–3950.
[28] Y. Hong, W. Ahn, S.V. Boriskina, X. Zhao, B.M. Reinhard, Directed assembly of optoplasmonic hybrid materials with tunable photonic–plasmonic properties, J. Phys. Chem. Lett. 6 (11) (2015) 2056–2064.
[29] D. Liu, C. Liu, Y. Yuan, X. Zhang, Y. Huang, S. Yan, Microfluidic transport of hybrid optoplasmonic particles for repeatable SERS detection, Anal. Chem. 93 (30) (2021) 10672–10678.

[30] J. Li, Y. Zhang, S. Ding, R. Panneerselvam, Z. Tian, Coree Shell nanoparticle enhanced Raman spectroscopy, Chem. Rev. 117 (2017) 5002e5069.
[31] Y.Z. Qin, Y.Z. Wu, B.J. Wang, J.Y. Wang, W.X. Yao, Facile synthesis of Ag@Au core-satellite nanowires for highly sensitive SERS detection for tropane alkaloids, J. Alloys Compd. 884 (2021), 161053.
[32] H.D. Trinh, S. Yoon, Silica-encapsulated Core−Satellite Au nanoparticle assemblies as stable, sensitive, and multiplex surface-enhanced Raman scattering probes, ACS Appl. Nano Mater. 5 (4) (2022) 5087–5095.
[33] W.M. Yang, M.M. Liang, G.Y. Sun, et al., Statistical strategy for quantitative evaluation of plasmon enhanced spectroscopy, ACS Photonics 9 (5) (2022) 1733–1740.
[34] Z. Cai, Y. Hu, Y. Sun, Q. Gu, P. Wu, C. Cai, Z. Yan, Plasmonic SERS biosensor based on multibranched Au nanoparticles embedded in polydimethylsiloxane for quantification of hematin in human erythrocytes, Anal. Chem. 93 (2) (2021) 1025–1032.
[35] L.L. Zhang, R. Hao, D. Zhang, et al., Shape-controlled hierarchical flowerlike Au nanostructure microarrays by electrochemical growth for surface-enhanced Raman spectroscopy application, Anal. Chem. 92 (14) (2020) 9838–9846.
[36] Y. Hong, M.L. Li, Z.H. Wang, B.Y. Xu, et al., Engineered opt plasmonic core-satellite microspheres for SERS determination of methamphetamine derivative and its precursors, Sensor. Actuator. B Chem. 358 (2022), 131437.
[37] K. Mao, Z.G. Yang, H. Zhang, X.Q. Li, M. Jonathan, Cooper Paper-based nanosensors to evaluate community-wide illicit drug use for wastewater-based epidemiology, Water Res. 189 (2021), 116559.
[38] W. Fang, B. Zhang, F.Y. Han, et al., On-site and quantitative detection of trace methamphetamine in urine/serum samples with a surface-enhanced Raman scattering active microcavity and rapid pretreatment device, Anal. Chem. 92 (19) (2020) 13539–13549.
[39] G.W. Kima, J.W. Ha, Retracted Article: single Au nanostars with multiple branches as multispectral orientation probes in single-particle rotational tracking, Chem. Commun. 57 (2021) 3263–3266.
[40] X. Fan, J.Z. Wang, H.B. Wang, X. Liu, H. Wang, Bendable ITO-free organic solar cells with highly conductive and flexible PEDOT: PSS electrodes on plastic substrates, ACS Appl. Mater. Interfaces 7 (30) (2015) 16287–16295.